

See discussions, stats, and author profiles for this publication at: <https://www.researchgate.net/publication/23315416>

# Block Copolymer Morphologies in Dye-Sensitized Solar Cells: Probing the Photovoltaic Structure-Function Relation

ARTICLE *in* NANO LETTERS · NOVEMBER 2008

Impact Factor: 13.59 · DOI: 10.1021/nl800942c · Source: PubMed

---

CITATIONS

105

---

READS

82

7 AUTHORS, INCLUDING:



Caterina Ducati

University of Cambridge

174 PUBLICATIONS 6,323 CITATIONS

SEE PROFILE



Sabine Ludwigs

Universität Stuttgart

75 PUBLICATIONS 1,961 CITATIONS

SEE PROFILE

# Block Copolymer Morphologies in Dye-Sensitized Solar Cells: Probing the Photovoltaic Structure–Function Relation

Edward J. W. Crossland,<sup>†,‡</sup> Mihaela Nedelcu,<sup>†</sup> Caterina Ducati,<sup>‡</sup>  
Sabine Ludwigs,<sup>†,§</sup> Marc A. Hillmyer,<sup>||</sup> Ullrich Steiner,<sup>\*,†</sup> and Henry J. Snaith<sup>\*,⊥</sup>

*Department of Physics, Cavendish Laboratories, University of Cambridge, Cambridge CB3 0HE, U.K., University of Cambridge Nanoscience Centre, Cambridge, CB3 0FF, U.K., Department of Materials Science & Metallurgy, University of Cambridge, Cambridge, CB2 3QZ, U.K., Department of Chemistry, University of Minnesota, Minneapolis, Minnesota 55455-0431, Department of Physics, University of Oxford, OX1 3PU, U.K., and Freiburg Institute for Advanced Studies (FRIAS), University of Freiburg, Germany*

Received April 3, 2008; Revised Manuscript Received September 22, 2008

## ABSTRACT

We integrate mesostructured titania arrays into dye-sensitized solar cells by replicating ordered, oriented one-dimensional (1D) columnar and three-dimensional (3D) bicontinuous gyroid block copolymer phases. The solar cell performance, charge transport, and recombination are investigated. We observe faster charge transport in 1D “wires” than through 3D gyroid arrays. However, owing to their structural instability, the surface area of the wire arrays is low, inhibiting the solar cell performance. The gyroid morphology, on the other hand, outperforms the current state-of-the-art mesoporous nanoparticle films.

A major goal of nanotechnology is to achieve enhanced and novel functionality by gaining control of nanoscale material architectures. The detailed morphology and orientation of these nanostructures are key parameters determining their effectiveness in real devices applications. Emerging solar energy technologies based on “excitonic” photovoltaic systems<sup>1</sup> are a prime example in which low-cost and highly processable material components rely on mutual nanoscale organization in order to deliver efficient performance. Two-component organic solar cells rely on exciton ionization at type-II semiconductor heterojunctions, requiring a high degree of interdigitation of the two components combined with continuous electrical conductivity of both phases to the respective electrodes. Dye-sensitized heterojunctions, on the

other hand, have a molecular absorbing component located directly at the interface itself and rely on the enormous surface area of a mesostructured semiconductor film to achieve sufficient optical density in the active layer. Both concepts call for a large interface in a two-component material coupled with mutually continuous transport pathways through the device to the external circuit.

Self-assembled morphologies are suitable candidates for ideal photovoltaic heterojunctions. Quasi-1D structures such as standing nanowire arrays have attracted particular interest owing to the possibility of direct charge extraction pathways throughout the device thickness.<sup>2–4</sup> The success of any structure is, however, a combination of many factors, such as charge transport and recombination kinetics, interfacial contact area, and structural stability. These parameters are determined both directly by the nature of the topology (for example direct vs tortuous conduction paths) and indirectly by intrinsic properties of the material (such as the density and location of defect sites) both of which are strongly affected by the structure fabrication process. In practice, probing the influence of structural morphology in a real working device is crucial since there are many unforeseen factors which will govern the performance of a given nanomorphology.

\* Corresponding authors, u.steiner@phy.cam.ac.uk and h.snaith1@physics.ox.ac.uk.

<sup>†</sup> Department of Physics, Cavendish Laboratories, University of Cambridge and University of Cambridge Nanoscience Centre.

<sup>‡</sup> Department of Materials Science & Metallurgy, University of Cambridge.

<sup>§</sup> Institute for Macromolecular Chemistry & Freiburg Materials Research Centre, University of Freiburg, Stefan-Meier-Str. 31, 79104 Freiburg, Germany.

<sup>||</sup> Department of Chemistry, University of Minnesota.

<sup>⊥</sup> Department of Physics, University of Oxford.

<sup>#</sup> FRIAS.

The effect of structure on device performance is difficult to isolate because of the different procedures usually required to create the various nanostructures. For instance the crystal size, defect density, and surface potential are likely to be very different between one-dimensional arrays of anodized titania nanotubes as compared to unoriented films fabricated from sol–gel processed sintered nanoparticles. One very promising way to produce a range of controlled and highly ordered morphologies in the same material system and on the same scale is to replicate self-assembled structures from sacrificial templating systems.<sup>5–7</sup> Diblock copolymers, consisting of two chemically distinct tethered polymer chains, exhibit self-assembly into a range of periodically ordered microphases on the 10 nm length scale. This class of material offers a unique toolbox for exploring nanotechnology applications since, with a given polymer chemical makeup, we have access to a number of microphase morphologies by simply tuning the relative volume fraction of each block.<sup>8,9</sup> Selective removal of one component of a block copolymer after phase separation leaves behind a mesoporous template.<sup>10</sup> For example, standing arrays of nanowires can be formed from cylinder-forming copolymers by first aligning the microphase in an external electric field.<sup>11,12</sup> Electrochemical deposition is a useful tool for replicating very high aspect ratio templates such as these where the pore structure is of the order of 10 nm through films hundreds of nanometers to micrometers in thickness.<sup>13,14</sup> We have recently demonstrated the electrochemical replication of the block copolymer bicontinuous gyroid phase using the same sacrificial approach.<sup>15</sup> We are now able therefore to replicate two functional material nanostructures with identical characteristic length scales ( $\sim 10$  nm) but with fundamentally different structural morphologies.

Here, we probe the performance of cylinder and gyroid network block-copolymer morphologies replicated in anatase titania, incorporated in liquid electrolyte dye-sensitized solar cells (DSCs). In this system, a molecular dye is used to sensitize a prestructured wide band gap inorganic metal oxide.<sup>16</sup> A liquid electrolyte containing a redox couple surrounds the structure and acts as an electron shuttle from the counter electrode to regenerate the oxidized dye molecule, thereby completing the circuit. The most extensively studied, and still most successful implementation of this device scheme utilizes a disordered mesoporous inorganic layer made up of sintered  $\text{TiO}_2$  nanoparticles with around 60% porosity. The charge collection efficiency in nanoparticulate  $\text{TiO}_2$  DSCs is high owing to an effective electron diffusion length much greater than the required device thickness to enable complete light absorption. This electrochemical system has been extensively modeled and studied experimentally and therefore provides an ideal testing ground for characterizing novel nanostructured electrodes. Our results for these systems are of particular importance for related DSC cell designs incorporating alternative hole transporting materials, such as solid-state molecular semiconductors, where the optimal device thickness remains far lower than the optical depth at peak absorbance.<sup>17,18</sup>

Two block copolymers of poly(4-fluorostyrene)-*b*-poly(D,L-lactide)(PFS-*b*-PLA) were synthesized as previously described.<sup>14</sup> The first sample ( $P_{\text{cyl}}$ ) had a molecular weight of  $41 \text{ kg mol}^{-1}$  and contained 65%<sub>mass</sub> PFS as determined by  $^1\text{H}$  NMR spectroscopy. The second sample ( $P_{\text{gyr}}$ ) had a molecular weight of  $36 \text{ kg mol}^{-1}$  and contained 60%<sub>mass</sub> PFS. The polydispersity indexes of  $P_{\text{cyl}}$  and  $P_{\text{gyr}}$  were determined by size exclusion chromatography as 1.15 and 1.21, respectively. Thin films of  $P_{\text{cyl}}$  and  $P_{\text{gyr}}$  were prepared by doctor-blade coating from toluene solutions onto conductive fluorine-doped tin oxide (FTO) glass substrates, which were precoated with a  $\sim 50$  nm thick compact layer of  $\text{TiO}_2$  by spray pyrolysis deposition.<sup>19</sup> The  $P_{\text{gyr}}$  films were annealed at  $180^\circ\text{C}$  in a  $\text{N}_2$  atmosphere for 35 h and allowed to cool to room temperature over 3 h. The electric field alignment of cylinder-forming PFS-*b*-PLA has been described previously.<sup>14</sup> In brief,  $P_{\text{cyl}}$ -coated substrates and a removable electrode were assembled into a parallel plate capacitor geometry and an electric field of  $\sim 120 \text{ V } \mu\text{m}^{-1}$  was applied across the copolymer film during a heating and cooling protocol which was otherwise identical to that of  $P_{\text{gyr}}$ . The removable counter electrode consisted of a  $25 \mu\text{m}$  thick gold-backed polyimide sheet (Kapton CR, Dupont) covered by a thermally cross-linked layer of poly(dimethylsiloxane) (PDMS) coating, which was employed to ensure a conformal contact with the copolymer films.<sup>11,20</sup> After the sample was annealed, the  $P_{\text{gyr}}$  films adopted the gyroid microphase morphology, while  $P_{\text{cyl}}$  formed a hexagonal PLA cylinder phase with cylinders spanning the film thickness. The normal orientation of the cylinders was a result of electric field alignment. No electric field was applied to  $P_{\text{gyr}}$ . This sample consisted of two intertwined, 3D PLA gyroid networks surrounded by PFS.

The PLA minority component was selectively removed from the copolymer films by immersion in a 0.05 M  $\text{NaOH}_{(\text{aq})}$  solution containing 40%<sub>vol</sub> MeOH at room temperature for several hours.<sup>21</sup> The resulting porous PFS films were used as templates for potentiostatic electrochemical growth of titanium(IV) oxide from 0.2 M aqueous  $\text{TiCl}_3$  at pH 2.7, containing 20%<sub>vol</sub> methanol in a standard three-electrode cell.<sup>22</sup> In order to remove the supporting PFS matrix with minimal mechanical perturbation to the templated Ti(IV) oxide nanostructures, the filled  $P_{\text{cyl}}$  films were first exposed to oxygen plasma for 200 s. The plasma exposed filled  $P_{\text{cyl}}$  films and the untreated filled  $P_{\text{gyr}}$  films were then heated to  $500^\circ\text{C}$  for 2 h on a hotplate under nitrogen, and for a further 1 h under oxygen. This treatment leads to crystallization of  $\text{TiO}_2$  and, in the case of the  $P_{\text{gyr}}$  composite films, the simultaneous oxidative removal of the polymer template. Thin films of nonstructured hydrated Ti(IV) oxide grown in this way exhibited a volume contraction of  $\sim 40\%$  when dried and crystallized.

Nanoparticle-based mesoporous titania films were made via doctor blade coating of a titania paste (20 nm nanoparticles) onto compact  $\text{TiO}_2$ -coated FTO glass, followed by slow heating to  $500^\circ\text{C}$  for 30 min in oxygen, as described previously.<sup>23</sup>

Scanning electron microscopy (SEM) characterizations of the three morphologies are shown in Figure 1. In the case

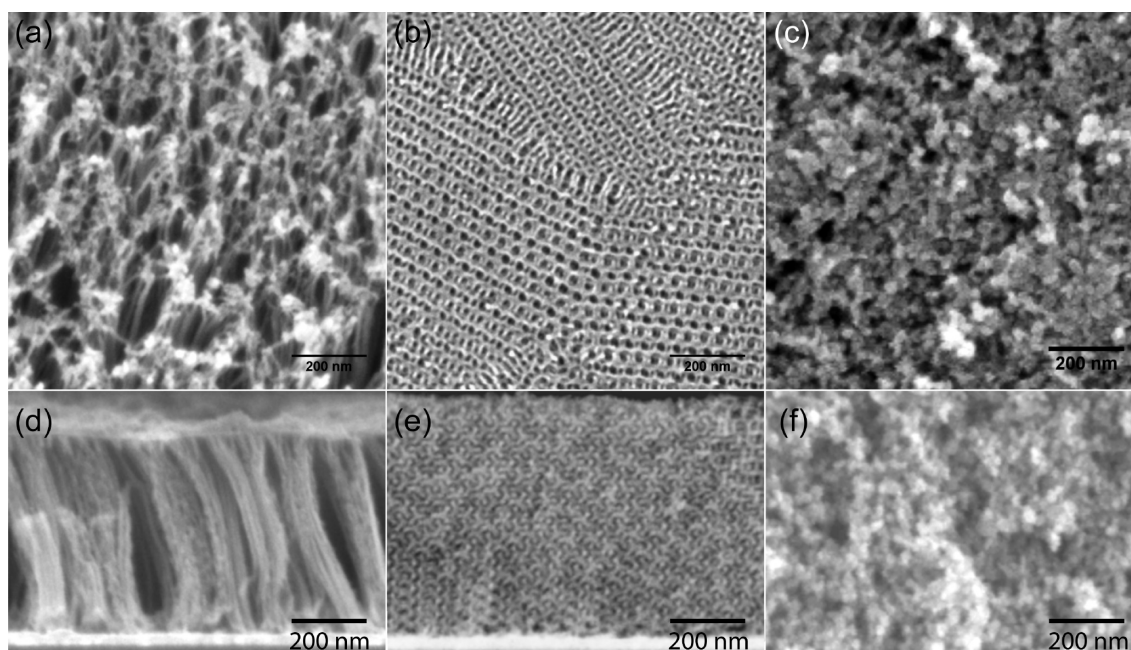


**Figure 1.** SEM of nanostructured array morphologies viewed from the top surface and cross-section perspectives. (a, d) Standing  $\text{TiO}_2$  cylinders. In (d), the wire stability is improved by a thin, partially continuous layer of electrochemical overgrowth at the array surface which hinders lateral collapse. (b, e) Gyroid network. (c, f) Sintered nanoparticle mesoporous layer.

**Table 1.** Summary of Calculated and Measured Roughness Factors for Each Array Morphology and Photovoltaic Performances in  $1.2 \mu\text{m}$  Liquid Electrolyte Cells under AM1.5 Illumination

morphology	$\text{RF}_{\text{calc}}^a$	$\text{RF}_{\text{meas}}^b$	porosity (%) <sup>c</sup>	$J_{\text{SC}}$ ( $\text{mA cm}^{-2}$ )	$V_{\text{OC}}$ (mV)	FF	$\eta$ (%)
wires	100	60	65	1.79	845	71	1.07
gyroid	125	130	60	5.83	713	71	2.97
particles	120	116 <sup>27</sup>	60	5.42	785	63	2.67

<sup>a</sup> Model calculations using “smooth” geometric constructions: wires, 12 nm diameter, 21 nm center-to-center hexagonal standing rods; cubic gyroid, 50 nm unit cell, consisting of cylindrical rods of 12 nm diameter; nanoparticles, 20 nm diameter spheres, 60% porosity with pointlike interparticle contact.

<sup>b</sup> Measured roughness factors: wires and gyroid, electrochemically accessible area of platinum replicated arrays. Particles, BET measured area of the mesoporous film. <sup>c</sup> Block copolymer porosity calculated from relative volume fractions of constituent blocks assuming densities of ( $\rho_{\text{PLA}} = 1.18 \text{ g cm}^{-3}$ )<sup>21</sup> and ( $\rho_{\text{PFS}} = 1.17 \text{ g cm}^{-3}$ ).

of  $\text{P}_{\text{cyl}}$  (Figure 1a), standing  $\text{TiO}_2$  nanowires are formed with a diameter of 12 nm, center-to-center separation of 21 nm, and hexagonal packing density of  $2.6 \times 10^{11} \text{ cm}^{-2}$ . The volume contraction in the wire films of  $\sim 25\%$  is accommodated by a reduction in thickness, determined by film profilometry and cross sectional SEM imaging. Replication of the  $\text{P}_{\text{gyr}}$  template (Figure 1b) produces a continuous interwoven  $\text{TiO}_2$  gyroid network with an approximate strut diameter of 12 nm. This assignment is supported by previous studies using grazing incidence small-angle X-ray scattering consistent with an  $Ia\bar{3}d$  50 nm cubic unit cell aligned with (211) planes parallel to the substrate with an accumulated uniaxial compression of 50% in the vertical direction after high-temperature annealing.<sup>15</sup> The nanoparticle film (Figure 1c) consists of a disordered mesoporous network of  $\sim 20 \text{ nm}$   $\text{TiO}_2$  particles with approximately 60% porosity.<sup>24</sup>

Estimates of the available surface area of each array can be calculated from a model topology assuming a smooth  $\text{TiO}_2$  surface (i.e., neglecting submesoscale roughness). The nanowire array is modeled as a hexagonally ordered array of cylinders with a 21 nm center-to-center distance and 12 nm diameter giving a surface multiplicity (“roughness factor” (RF)) of  $100/\mu\text{m}$ . A simple cylindrical rod model can be used to approximate the gyroid morphology;<sup>25</sup> Assuming a rod

diameter of 12 and 50 nm cubic unit cell predicts a RF of  $125/\mu\text{m}$ . Finally, modeling the nanoparticle film as a 60% porous assembly of 20 nm spheres yields a RF of  $120/\mu\text{m}$ .

Measurements of the wire and gyroid array surface areas were made via the electrochemically accessible area for proton adsorption using identical morphologies replicated in platinum.<sup>26</sup> These arrays were made by potentiostatic deposition into the same templates at 0.1 V vs Ag/AgCl in a 20 mM  $\text{H}_2\text{PtCl}_{6(\text{aq})}$  solution containing 20%<sub>vol</sub> methanol. The PFS templates were removed by 200 s  $\text{O}_2$  plasma etching. The charge associated with proton adsorption was recorded in a 0.1 M  $\text{H}_2\text{SO}_{4(\text{aq})}$  solution as previously described.<sup>15</sup> The measured roughness factors of the wires and gyroid arrays were 60 and 130, respectively. The surface area of identical nanoparticle arrays to those used here have been measured by nitrogen adsorption giving a roughness factor of 116.<sup>27</sup> The calculated and measured roughness factors are summarized in Table 1. Both the nanoparticle and gyroid network structures have measured internal surface areas in good agreement with the predicted value, demonstrating that these structures form robust self-supporting networks which remain stable when incorporated into the device geometry. The nanowire array however has only 60% of the predicted RF, indicating a loss in real surface, likely to be due to



neighboring wires touching after removal of the template matrix.

High-resolution transmission electron microscopy was used to probe the  $\text{TiO}_2$  crystal phase and characteristic grain size in each of the three morphologies (Figure 2). Atomic lattice fringes and large area electronic diffraction rings were indexed to anatase  $\text{TiO}_2$  in all cases. Parts a and b of Figure 2 show that for both the wires and gyroid structure the crystallite size is of the same order as the structural confinement ( $\sim 10$  nm). In the wire structures the crystallite dimensions appear to exceed this confinement length along the wire axis in some places (Figure 2a inset). The disordered nanoparticle network (Figure 2c) is made up of  $\sim 20$  nm randomly contacted single crystal anatase nanoparticles.

The performance of the three array morphologies was tested in liquid electrolyte dye-sensitized solar cells. Anatase titania arrays of  $\sim 1.2$   $\mu\text{m}$  in thickness were prepared and first subjected to a standard surface treatment by soaking in aqueous  $\text{TiCl}_4$  solution (40 mM) at 80  $^\circ\text{C}$  for 30 min, with subsequent annealing at 500  $^\circ\text{C}$  for 30 min.<sup>27</sup> After cooling to 70  $^\circ\text{C}$  the arrays were immersed overnight in an acetonitrile:*tert*-butyl alcohol (1:1 vol:vol) 0.5 mM solution of bipyridyl NCS ligand ruthenium complex dye, termed N719. Closed cells were assembled with a Pt-coated FTO counter electrode and "Robust" liquid electrolyte (0.8 M PMII, 0.15 M iodine, 0.1 M GuNCS, and 0.5 M NMBI in 3-methoxypropionitrile) was infiltrated into the cell via vacuum back-filling.<sup>28</sup>

Figure 3a shows the absorption spectra of the N719 sensitized arrays before cell construction. Both the gyroid and wire spectra show vertical offsets caused by scattering in the titania array. When considering the peak OD of each array corrected for the scattering offset at 800 nm, the nanoparticle and gyroid arrays have comparable degrees of dye loading. The nanowire structure, on the other hand, has only half the peak OD seen in the gyroid and particle arrays, indicating a considerably lower accessible area in the actual device geometry for dye uptake.

The solar cell performance was characterized as described in the Supporting Information. The spectral responses of liquid electrolyte DSCs based on the three array structures are shown in Figure 3b. At low illumination intensities ( $\sim 0.1$   $\text{mW cm}^{-2}$ ) the nanoparticle film shows the highest peak external quantum efficiency (EQE) of 34% compared to 28% for the gyroid array. The nanowire cell produces a peak EQE of just 9%. Figure 3c shows the current–voltage curves for the cells under simulated AM 1.5 illumination at 100  $\text{mW cm}^{-2}$ . The device performances are summarized in Table 1. The gyroid, nanoparticle, and nanowire cells have power conversion efficiencies of 3.0, 2.7, and 1.1%, respectively. Considering the nanowire-based device, the combination of relatively weak adsorption, EQE and power conversion efficiencies are consistent with a low dye loading. Indeed, the measured roughness factor for a nanowire array was only 60% of the predicted value of 100/ $\mu\text{m}$  (Table 1) for a perfect standing array. A second reason for the low power conversion efficiency may arise from the one-dimensional nature of these extremely high aspect ratio structures ( $\sim 100$ ); physical

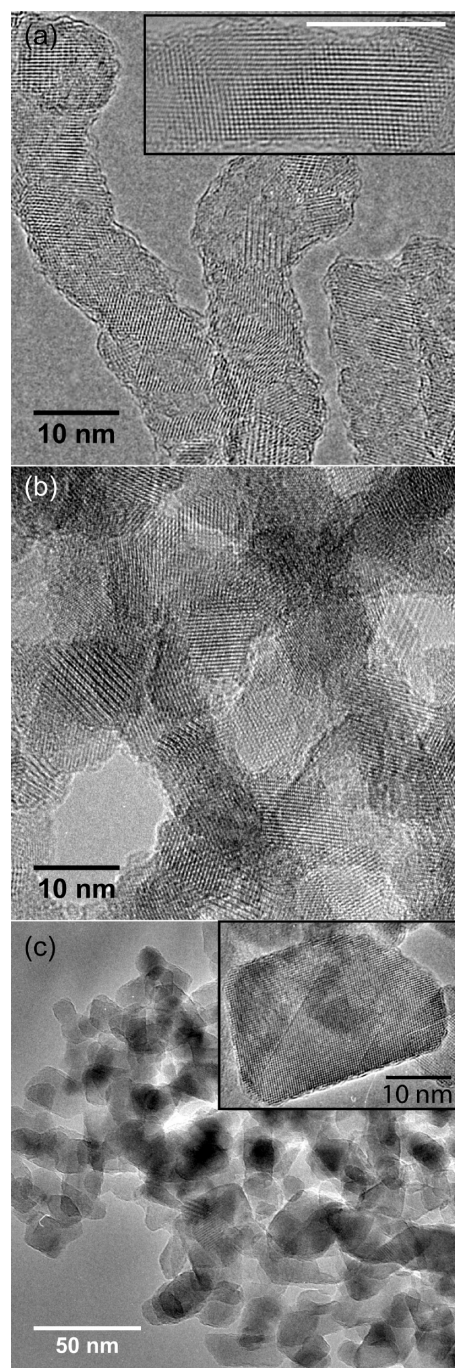


**Figure 2.** HRTEM images of crystal structure within  $\text{TiO}_2$  arrays: (a) nanowires; (b) gyroid network; (c) nanoparticles. The lattice fringes can be indexed to anatase  $\text{TiO}_2$ . In both wires and gyroid structure the crystallite size is of the same order as the structural confinement ( $\sim 10$  nm). In some wire structures individual crystal domains persist along the wire growth direction ((a) inset, scale bar 10 nm). The low-magnification view of the nanoparticle array in (c) reveals the disordered packing of  $\sim 20$  nm individual particles into a mesoporous layer, while a high-magnification view (inset) on the same scale as (a) and (b) indicates that the nanoparticles are single domain anatase crystallites.

damage to a wire during processing could prevent collection of any charge above the level of the fracture. This loss mechanism alone, however, does not explain the lower than expected dye loading and therefore does not appear to be a dominant factor here.

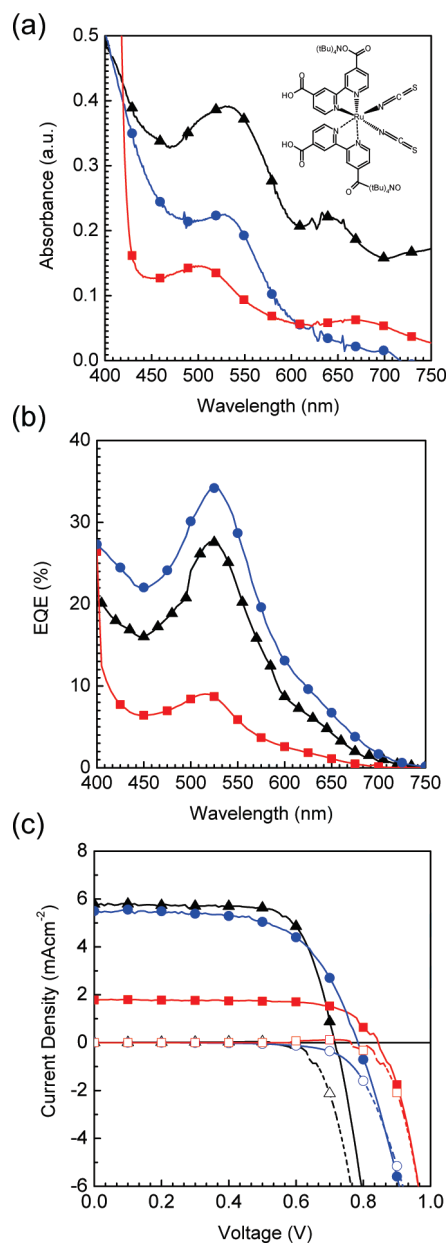


**Figure 3.** Solar cell characteristics for 1.2  $\mu\text{m}$  thick nanowire (solid red box), 1.2  $\mu\text{m}$  thick gyroid (solid black triangle) and 1.4  $\mu\text{m}$  thick nanoparticle (solid blue circle)  $\text{TiO}_2$  arrays. (a) Absorption spectra after sensitization with N719 (inset). (b) Spectral response of liquid electrolyte dye-sensitized solar cells. (c) Current–voltage curves under simulated AM 1.5 solar illumination at an intensity of  $100 \text{ mW cm}^{-2}$  (full lines) and in the dark (dashed lines).

There are significant differences in the open-circuit voltages of the devices incorporating these three different morphologies. The electrolyte and dye for all three systems are identical; however the  $\text{TiO}_2$  fabrication protocols for the diblock structured films and the nanoparticle based films are vastly different. Among many other factors, the open-circuit voltage is very sensitive to changes in surface potential of the  $\text{TiO}_2$ , which is dependent upon defect density, location, impurities, crystal size, and fabrication protocol. Hence, here we will make no comparison between the open-circuit voltage generated from the nanoparticle array and the other two morphologies. In contrast, comparing the gyroid and wire

arrays is justifiable, and indeed the purpose of this study, since these films were fabricated in identical manners. There is clearly a positive shift in the dark current turn on voltage which explains the increase in open-circuit voltage when going from gyroid to wires. We assume the cause for this positive shift is not due to a change in the surface potential of the  $\text{TiO}_2$  since the films have been fabricated in identical manners; therefore the larger surface area of the gyroid film is likely to be responsible for the increased dark current, with the current being limited by recombination (or electron/hole injection) at the  $\text{TiO}_2/\text{dye}/\text{electrolyte}$  interface. We will discuss this further below where we investigate the charge recombination lifetimes.

The power conversion efficiency of the gyroid network device (3.0%) is slightly greater than the nanoparticle array (2.7%) in the liquid electrolyte cell. These roughly comparable performances are not surprising considering the similar light-harvesting ability of the layers. The measured internal surface areas of the film are similar (RF gyroid 130, nanoparticles 116), which is reflected in the similar peak OD of N719 sensitized gyroid and nanoparticle arrays. The significant enhancement in performance of both the nanoparticle and gyroid device over the nanowire cell is most likely due to the structural stability of the network structure.

The electron transport and recombination properties of the three DSC arrays were probed by transient photocurrent and photovoltage spectroscopy.<sup>29,30</sup> The photocurrent decay rate at short-circuit is characteristic of the time for electron transport out of the device while the voltage decay rates at open-circuit are proportional to the rate of charge recombination.<sup>31</sup> The short-circuit charge collection times are shown in Figure 4a.

Charge transport in mesoporous titania is expected to be governed by a multiple-trapping process, where the electrons thermally detrapp from sub-bandgap states to the conduction band, and are transported a short distance before being retrapped.<sup>29</sup> However, the location of the traps, trap densities, and limitations to transport are still debatable and are almost certainly variable between different titania preparation routes.<sup>17</sup> With all other parameters equal, and assuming that electron motion is a random walk between uniformly distributed trap sites, idealized one-dimensional diffusion should be three times faster than in a fully three-dimensional case.<sup>32</sup> The scale on which the dimensionality of the mesostructure plays a role will depend upon the exact limiting factors to charge transport and electronic structure of the material. For instance if the transport is limited by scattering at grain boundaries, then the dimensionality needs to be on the order of the crystal size. If the transport is limited by detrapping throughout the material irrespective of grain boundaries, then the dimensionality would be required to be on the intertrap lengthscale. Here, the charge collection times measured in the wire arrays are approximately twice as fast as those in the gyroid networks under  $100 \text{ mW cm}^{-2}$  illumination. With identical structural sizes and fabrication protocols, it seems reasonable to expect comparable trap densities in both the wire and gyroid structures. In this case the transport performance of the wires is slightly below the



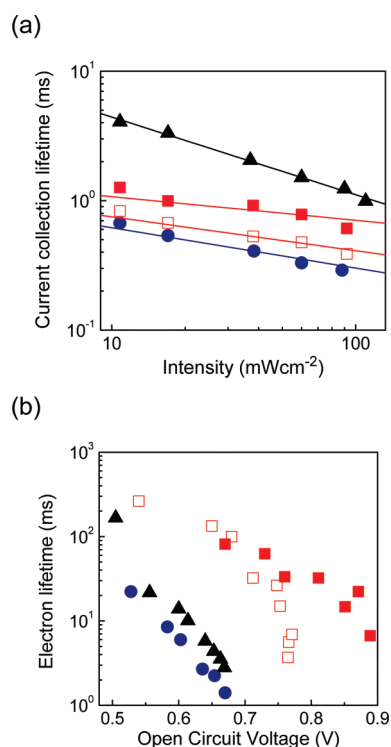


**Figure 4.** Current collection lifetimes for the samples in Figure 3. The second nanowire-array data set (open red box) is shown to illustrate the variation in transport response from this type of device. (b) Recombination lifetimes for the arrays shown in (a) measured at open circuit, plotted as a function of cell voltage.

3-fold improvement predicted for ideal 1D transport. This could be due to a number of reasons: Electronically, the trap density may be greater than one per nanocrystal. Physically, contacts exist between some of the wires and because the wires are not self-supporting there is a degree of disorder in their alignment in the standing array. The two data sets included in Figure 4 are indicative of the spread in measured collection times for the wire arrays.

The transport times in the disordered nanoparticle films are approximately four times faster than those in the 3D gyroid networks and roughly 40% faster than those in the nanowire arrays. Considering dimensionality and uniformity of the gyroid mesostructure, this is not expected. However, Kopidakis et al. have demonstrated a strong dependence of electron diffusion with crystal size<sup>33</sup> and the standard nanoparticles used here are approximately twice as large as the nanocrystallites in the electrochemically deposited films. The fabrication procedure for the particulate titania films is very different, and one would expect the trap density and location to vary considerably. Therefore, quantitative comparison between the particle and electrochemically deposited materials is not justified.

The recombination lifetime at open circuit is plotted in Figure 4b. Here, we plot the electron lifetime versus the open-circuit voltage since this is likely to be most representative of comparable charge densities within the devices. In the Supporting Information, we also show the electron lifetime plotted against incident light intensity in which the trends are unaltered. Interestingly, both the gyroid and the

nanowire devices exhibit longer electron lifetimes than the standard nanoparticle device. And, most significantly, the nanowire film has up to an order of magnitude longer electron lifetime than both the gyroid and the particle devices at any given voltage. Again, the exact spatial distribution of trap sites is likely to be critical; for the nanoparticle films, a large surface trap density is likely. Electrons residing on the particle surface have a greater likelihood of recombining with a hole in the electrolyte than electrons trapped within the bulk of the structures. The HRTEM images of the electrochemically deposited materials show that there is a large “internal” contact area between nanocrystalline domains. Recombination between charges trapped in defect sites at these contacts and holes in the electrolyte will be very slow. Furthermore, surface area, dye uptake, and SEM studies of nanowire films show a degree of structural collapse. We have observed that there is less than expected surface area available for dye loading. If these “self-contacting” regions are not contacted by electrolyte, then charges trapped on the internal surfaces of the wire bundles will be inhibited from recombination. Slower recombination kinetics in oriented wires are consistent with behavior observed in TiO<sub>2</sub> nanotube arrays by Zhu et al.<sup>34</sup> However, this is again likely to be due to the crystal “packing” and location of trap sites, rather than a direct consequence of the ordered structure. An interesting concept which follows from this observation is to design nanowire arrays with a large “internal” trap density. This would enable the electrons to travel between sites located far from the dye/electrolyte interface, in order to inhibit recombination.

In summary, we have fabricated free-standing arrays of 1D titania nanowires and 3D gyroid structured titania films by employing diblock copolymer templates. Integration of these films into dye-sensitized solar cells yields important information concerning the charge transport in mesostructured material composites. Although the 1D system exhibited enhanced charge transport and significantly inhibited charge recombination compared to an equivalent 3D network, the lack of structural integrity resulted in a much reduced internal surface area compared to the conceptually ideal structure, and the resulting photocurrent and efficiency generated from the solar cells were significantly less than the 3D gyroid devices. In future work we will therefore seek to improve the mechanical stability of wire-type systems to exploit their excellent electronic properties, and enhance the electronic properties of three dimensionally structured semiconductor arrays, to capitalize upon their superior structural integrity. These results are the first exploratory study comparing two key block copolymer morphologies in functioning devices, demonstrating the complex interplay of factors determining ideal morphologies for bulk heterojunctions. Further studies of this type, investigation of different material systems, and further structural refinement should greatly enhance our understanding of the role of nanoscale structure upon this new generation of optoelectronic devices.

**Acknowledgment.** This work was supported by EPSRC, the National Science Foundation, the Leverhulme Trust, and the European RTN-6 Network “Polyfilm”. H.J.S. thanks

Clare College Cambridge for funding. C.D. acknowledges the Royal Society for financial support. We thank Daniel Corbett, Burak Ulgut, and Richard Friend for valuable discussions and support. Correspondence and requests for materials should be addressed to U.S. (u.steiner@phy.cam.ac.uk) or H.J.S. (h.snaith1@physics.ox.ac.uk).

**Supporting Information Available:** Description of solar cell characterization and plot of electron lifetime vs light intensity. This material is available free of charge via the Internet at <http://pubs.acs.org>.

## References

- (1) Gregg, B. A. *J. Phys. Chem. B* **2003**, *107*, 4688.
- (2) Law, M.; Greene, L. E.; Johnson, J. C.; Saykally, R.; Yang, P. *Nat. Mater.* **2005**, *4*, 455.
- (3) Mor, G. K.; Shankar, K.; Paulose, M.; Varghese, O. K.; Grimes, C. A. *Nano Lett.* **2006**, *6*, 215.
- (4) Kongkanand, A.; Tvrdy, K.; Takechi, K.; Kuno, M.; Kamat, P. V. *J. Am. Chem. Soc.* **2008**, *130*, 4007.
- (5) Bae, C.; Yoo, H.; Kim, S.; Lee, K.; Kim, J.; Sung, M. A.; Shin, H. *Chem. Mater.* **2008**, *20*, 756.
- (6) Olson, D. A.; Chen, L.; Hillmyer, M. A. *Chem. Mater.* **2008**, *20*, 869.
- (7) Thomas, A.; Goettmann, F.; Antonietti, M. *Chem. Mater.* **2008**, *20*, 738.
- (8) Hamley, I. W. *The physics of block copolymers*; Oxford University Press: Oxford, 1998.
- (9) Bates, F. S.; Fredrickson, G. H. *Phys. Today* **1999**, 32–38.
- (10) Hillmyer, M. A. *Adv. Polym. Sci.* **2005**, *190*, 137.
- (11) Thurn-Albrecht, T.; Steiner, R.; DeRouchey, J.; Stafford, C.; Huang, E.; Bal, M.; Tuominen, M.; Hawker, C.; Russell, T. *Adv. Mater.* **2000**, *12*, 787.
- (12) Xu, T.; Zvelindovsky, A. V.; Sevink, G. J. A.; Lyakhova, K. S.; Jinnai, H.; Russell, T. P. *Macromolecules* **2005**, *38*, 10788.
- (13) Thurn-Albrecht, T.; Steiner, R.; DeRouchey, J.; Stafford, C. M.; Huang, E.; Bal, M.; Tuominen, M.; Hawker, C. J.; Russell, T. P. *Adv. Mater.* **2000**, *12*, 787.
- (14) Crossland, E. J. W.; Ludwigs, S.; Hillmyer, M. A.; Steiner, U. *Soft Matter* **2007**, *3*, 94.
- (15) Crossland, E. J. W.; Kamperman, M.; Nedelcu, M.; Ducati, C.; Wiesner, U.; Ludwigs, S.; Smilgies, D. M.; Toombes, G. E. S.; Hillmyer, M. A.; Steiner, U.; Snaith, H. J. 2008Submitted for publication.
- (16) O'Regan, B.; Grätzel, M. *Nature* **1991**, *353*, 737.
- (17) Snaith, H. J.; Schmidt-Mende, L. *Adv. Mater.* **2007**, *19*, 3187.
- (18) Grätzel, M. *MRS Bull.* **2005**, *30*, 23.
- (19) Kavan, L.; Grätzel, M. *Electrochim. Acta* **1995**, *40*, 643.
- (20) Thurn-Albrecht, T.; Schotter, J.; Kastle, G.; Emley, N.; Shibauchi, T.; Krusin-Elbaum, L.; Guarini, K.; Black, C. T.; Tuominen, M. T.; Russell, T. P. *Science* **2000**, *290*, 2126.
- (21) Zalusky, A. S.; Olayo-Valles, R.; Wolf, J. H.; Hillmyer, M. A. *J. Am. Chem. Soc.* **2002**, *124*, 12761.
- (22) Kavan, L.; O'Regan, B.; Kay, A.; Grätzel, M. *J. Electroanal. Chem.* **1993**, *346*, 291.
- (23) Snaith, H. J.; Schmidt-Mende, L.; Grätzel, M. *Phys. Rev. B* **2006**, *74*, 045306.
- (24) Barbe, C. J.; Arendse, F.; Comte, P.; Jirousek, M.; Lenzmann, F.; Chklover, V.; Grätzel, M. *J. Am. Ceram. Soc.* **1997**, *80*, 3157.
- (25) Luzzati, V.; Spegt, P. A. *Nature* **1967**, *215*, 701.
- (26) Trasatti, S.; Petrii, O. A. *J. Electroanal. Chem.* **1992**, *327*, 353.
- (27) Ito, S.; Liska, P.; Comte, P.; Charvet, R.; Pechy, P.; Bach, U.; Schmidt-Mende, L.; Zakeeruddin, S. M.; Kay, A.; Nazeeruddin, M. K.; Grätzel, M. *Chem. Commun.* **2005**, 4351–4353.
- (28) Kuang, D.; Ito, S.; Wenger, B.; Klein, C.; Moser, J.; Humphry-Baker, R.; Zakeeruddin, S. M.; Grätzel, M. *J. Am. Chem. Soc.* **2006**, *128*, 4146.
- (29) Frank, A. J.; Kopidakis, N.; van de Lagemaat, J. *Coord. Chem. Rev.* **2004**, *248*, 1165.
- (30) O'Regan, B.; Lenzmann, F. *J. Phys. Chem. B* **2004**, *108*, 4342.
- (31) Snaith, H. J.; Moule, A. J.; Klein, C.; Meerholz, K.; Friend, R. H.; Grätzel, M. *Nano Lett.* **2007**, *7*, 3372.
- (32) Zhu, K.; Neale, N. R.; Miedaner, A.; Frank, A. J. *Nano Lett.* **2007**, *7*, 69.
- (33) Kopidakis, N.; Neale, N. R.; Zhu, K.; van de Lagemaat, J.; Frank, A. J. *Appl. Phys. Lett.* **2005**, *87*, 202106.
- (34) Zhu, K.; Vinzant, T. B.; Neale, N. R.; Frank, A. J. *Nano Lett.* **2007**, *7*, 3739.

NL800942C